



Mechanisms of aqueous bromate reduction activity enhancement with well-defined bimetallic palladium-based catalysts

Jacob P. Troutman ^{a,b,1}, João Restivo ^{c,d,1}, Hyunwoo Ha ^b, Zahra Bajalan ^b, Carolyn E. Brady ^{a,b}, João M.B. Costa ^{c,d}, Carolina Vigil-Hernandez ^b, José R.M. Barbosa ^{c,d}, Carla A. Orge ^{c,d}, Manuel F.R. Pereira ^{c,d}, Simon M. Humphrey ^b, Graeme Henkelman ^{b,*}, Charles J. Werth ^{a,*}, Olívia S.G.P. Soares ^{c,d,**}

^a Department of Civil, Architectural, and Environmental Engineering, The University of Texas at Austin, Austin, TX 78712, United States

^b Department of Chemistry, The University of Texas at Austin, Austin, TX 78712, United States

^c LSRE-LCM - Laboratory of Separation and Reaction Engineering - Laboratory of Catalysis and Materials, Faculty of Engineering, University of Porto, Porto 4200-465, Portugal

^d ALiCE - Associate Laboratory in Chemical Engineering, Faculty of Engineering, University of Porto, Rua Dr. Roberto Frias, Porto 4200-465, Portugal

ARTICLE INFO

Keywords:

Bimetallic alloy catalysts

Bromate reduction

Water treatment

Density functional theory (DFT)

ABSTRACT

Catalytic reduction has been shown to remove bromate (BrO_3^-) in drinking water without waste stream formation, though most reported catalysts rely on palladium (Pd), a financially and environmentally expensive metal. Emerging efforts show Pd can be partially replaced with less expensive metals in nanoparticle (NP) alloys, with enhanced hydrogenation reactivity. However, it is unclear if novel NP alloys will enhance bromate reduction, and if so whether they can be intelligently designed based on underlying mechanisms of enhancement. Herein, we address this knowledge gap reporting that well-defined alloyed PdCu and PdAg nanoparticles deposited on carbon nanotubes achieve a 3.9-times improvement in catalytic activity versus monometallic Pd catalysts, which further translates to catalysts prepared using straight-forward impregnation methods. Density functional theory results indicate that improved hydrogenation rates are related to optimized BrO_3^- and H binding on PdM surfaces achieved by electronic effects in PdCu alloys and unique surface ensembles in PdAg alloys. Overall, these catalysts delineate a pathway for improved bromate removal activity at environmentally relevant concentrations.

1. Introduction

Ozonation is a commonly used practice in drinking water and wastewater treatment. Ozone serves as an oxidizing agent and disinfectant; it can improve the odour and taste of finished drinking water, and it reduces turbidity in filtered water by facilitating flocculation [1–3]. However, many surface and groundwater sources contain bromide (Br^-), which derives from the discharge of sewage and industrial effluent, crop irrigation with methyl bromide, de-icing salt run-off, and the dissolution of naturally occurring bromine-containing minerals [4]. During ozonation, Br^- and bromine-containing species can be oxidized to bromate (BrO_3^-) and other brominated disinfection by-products

(DBPs) [1,5]. BrO_3^- and these DBPs are linked to multiple health concerns, and the World Health Organization (WHO) has set the maximum BrO_3^- concentration at $10 \mu\text{g L}^{-1}$ in drinking water [6]. Given that ozonation is a critical process in drinking and wastewater treatment, the lack of techniques to adequately control BrO_3^- formation or to promote its removal has led to increasing interest in BrO_3^- removal technologies [4,7].

Current solutions to remove BrO_3^- , such as ion-exchange [8], adsorption using traditional adsorbents like activated carbon [9] or more advanced materials such as covalent organic frameworks (COFs) [10], and reverse osmosis [11], rely on the separation and concentration of BrO_3^- into secondary liquid or solid waste streams. However, this

* Corresponding authors.

** Corresponding author at: LSRE-LCM - Laboratory of Separation and Reaction Engineering - Laboratory of Catalysis and Materials, Faculty of Engineering, University of Porto, Porto 4200-465, Portugal.

E-mail addresses: henkelman@utexas.edu (G. Henkelman), werth@utexas.edu (C.J. Werth), salome.soares@fe.up.pt (O.S.G.P. Soares).

¹ These authors contributed equally to this work.

secondary waste stream requires additional treatment or disposal [4,12, 13]. Strategies to reduce BrO_3^- back to Br^- via microbial species in biological reactors [14], photocatalysis [15], (electro)chemical reduction with zero-valent iron [16,17], sulphite reduction [18] or catalytic hydrogenation [19] have proven promising. However, these solutions still require further development for effective translation to practical applications. Challenges include concerns of pathogenic growth during treatment, poor efficiency, reliance on expensive materials and a lack of understanding under environmentally relevant matrices and concentration levels (e.g., in the range of 10's–100's $\mu\text{g L}^{-1}$ in natural waters) [4].

Catalytic reduction using hydrogen as the electron donor is one of the most efficient alternatives for the chemical reduction of BrO_3^- in water [19–22]. However, like other BrO_3^- mitigation strategies, there are still open questions regarding its behaviour in natural waters, its performance at $\mu\text{g L}^{-1}$ levels and costs associated with the use of expensive platinum-group metal catalysts [23]. Efforts to improve the performance of catalytic systems are often carried out by tuning catalyst design towards faster kinetics through the selection of an adequate metal catalyst phase [19]. Platinum-group metals (PGMs), like palladium (Pd) and platinum (Pt), are most commonly used, though they are expensive and can present a high risk for replacement if catalyst fouling or poisoning is anticipated. The use of non-PGM catalysts based on titanium carbide (TiC) [24], cobalt (Co) [25,26] or manganese (Mn) [27] has also been explored to reduce costs, as has the introduction of secondary metals to PGM catalysts [28]. Regarding the latter, it has been demonstrated that alloying a PGM (generally Pd) with a non-active metal (e.g., copper (Cu), silver (Ag) or gold (Au)) improves the performance per cost of bimetallic catalysts in the hydrogenation of nitrite (NO_2^-). The improvement in activity has been attributed to d-band mixing and local atomic ensembles on the surface of the catalyst that alter the binding energies for hydrogen atoms and reactants on the PGM, thus lowering the overall free energy of hydrogenation and increasing the rate of reaction [29–31]. Additionally, the introduction of Ag or Cu also has the potential to reduce the overall cost of the catalyst material given the comparative costs of Ag and Cu versus Pd (0.66 € $\text{g}_{\text{Ag}}^{-1}$ versus 0.0085 € $\text{g}_{\text{Cu}}^{-1}$ versus 46.65 € $\text{g}_{\text{Pd}}^{-1}$; APMEC, Inc. and MoneyMetals.com, February 2023). Bimetallic Pd-based catalysts have also been used to improve catalyst performance for aqueous bromate reduction, but the mechanism for this activity enhancement has not been elucidated [21,22,28]. Alternative catalyst supports have also been used to improve performance for aqueous bromate reduction [20,22,32–34], but are not the focus of this effort.

In this work, we utilize well-defined bimetallic palladium–copper nanoparticles ($\text{Pd}_x\text{Cu}_{100-x}\text{NPs}$) and palladium–silver nanoparticles ($\text{Pd}_x\text{Ag}_{100-x}\text{NPs}$) supported on multiwalled carbon nanotubes (MWCNTs) paired with density functional theory (DFT) calculations to investigate the mechanism by which incorporating a non-precious (Cu) or semi-precious (Ag) metal enhances aqueous bromate reduction kinetics in drinking water treatment settings. Monometallic Pd nanoparticles (PdNPs) and alloyed $\text{Pd}_x\text{M}_{100-x}\text{NPs}$ ($\text{M} = \text{Cu}$ or Ag) with target compositions of $x = 75, 50$ and 25 were synthesized using a microwave-assisted polyol technique because of the high degree of compositional and structural control afforded by this method compared to alternative strategies [29,35,36]. The as-synthesized NPs were then characterized and deposited on MWCNTs for evaluation of BrO_3^- reduction activity in semi-open batch reactors using nanopure water with environmentally relevant BrO_3^- concentrations ($\mu\text{g L}^{-1}$) near circumneutral pH (i.e., pH 6.0). MWCNTs were chosen as the catalyst support material because they do not adsorb BrO_3^- [20], and catalysts supported on MWCNTs have demonstrated significant activity improvements for BrO_3^- reduction versus powdered activated carbon supports using the same metal active phase [20,37]. We combined these experimental results with DFT calculations to understand how alloying Pd with Cu or Ag impacts the BrO_3^- reduction at a molecular level, which is the first reporting of DFT calculations to examine aqueous bromate reduction. Lastly, we apply the

insights gained from the model nanoparticle catalysts to guide the synthesis of analogous catalysts using incipient wetness co-impregnation with either Pd(II) and Cu(II) or Pd(II) and Ag(I) precursors on MWCNTs; we probe both the structure and bromate reduction kinetics of these catalysts to determine if the same insights gained from model nanoparticles can be applied to conventionally synthesized catalysts so scale up to water treatment applications is feasible.

2. Experimental methods

2.1. Catalyst synthesis

2.1.1. Synthesis and deposition of bimetallic nanoparticle catalysts

Pd-based alloy nanoparticles ($\text{Pd}_x\text{M}_{100-x}\text{NPs}$, $\text{M} = \text{Ag}$ or Cu) were synthesized using a microwave(μw)-assisted polyol method previously published [29,35,36,38]. Microwave heating allows for more control over the nucleation and growth stages of nanoparticle formation compared to conventional heating methods (e.g., oil bath heating), imparting more uniformity in the resulting nanoparticles and better control over the nanoparticle shape [35,39]. All μw reactions were performed in a MARS 5 microwave reactor (CEM Corp.; 2.45 GHz; max power 1600 W). The reactions were carried out with a fibre-optic temperature feedback control (RTP300+ temperature sensor; CEM Corp.) with magnetic stirring (450 rpm) open to air. The reaction flask for all reactions consisted of a 50 mL one-neck round bottom flask fitted with a water-cooled reflux condenser. The metal precursor(s) were dissolved in ethylene glycol (EG) or water and then added at a controlled rate to a round bottom flask containing poly(vinylpyrrolidone) (PVP) in EG. The reaction was heated for an additional 30 min, before being quenched via an ice-water bath. The resulting nanoparticles were isolated by the addition of acetone, followed by centrifugation, and then pouring off the solvent. Excess PVP was removed by redispersing the NPs in a minimal amount of ethanol with sonication. The nanoparticles were recollected by adding hexanes, centrifuging and pouring off the solvent. The particles were then left to air dry overnight and stored as a glassy film in 50 mL polypropylene tubes. See [Supporting Information](#) page 1–2 and [Fig. S1](#) for more details.

Synthesized $\text{Pd}_x\text{M}_{100-x}\text{NPs}$ were loaded onto multi-walled carbon nanotube (MWCNTs) supports using direct deposition, which is known to preserve particle shape and dispersity [40,41]. In a 20 mL glass scintillation vial, MWCNTs (Nanocyl NC7000; 250 mg) were dispersed in distilled water (10 mL) using sonication and magnetic stirring (1200 rpm). Simultaneously, NPs (ca. 5 mg) were dispersed in ethanol (10 mL) with sonication. The NP suspension was then added dropwise to the support suspension. Following the addition, the mixtures were stirred (800 rpm; 10 min) and sonicated (10 min) for three cycles to ensure deposition. The slurry was vacuum filtered, and the clear supernatant disposed. The catalysts were washed with water and ethanol before being dried overnight at 60 °C.

2.1.2. Traditional synthesis of bimetallic catalysts

Supported catalysts were also synthesized using the well-established incipient wetness impregnation method [42]. In brief, MWCNTs were degassed in an ultrasonic bath for 30 min, after which an aqueous solution of the desired metallic precursor(s) (PdCl_2 , $\text{Cu}(\text{NO}_3)_2 \cdot 3 \text{ H}_2\text{O}$ and/or AgNO_3) was added dropwise to the support. The PdCl_2 was dissolved in a 37% HCl solution to facilitate dissolution. Solvent amount was determined by measurement of the maximum solvent volume completely absorbed by the selected mass of the catalyst support. An appropriate mass of PdCl_2 , $\text{Cu}(\text{NO}_3)_2 \cdot 3 \text{ H}_2\text{O}$ and/or AgNO_3 was used to achieve the target final catalyst loading of the desired metal(s). The wet support was then kept in the ultrasonic bath for 90 min, after which it was dried overnight at 100 °C. The dried solid was then calcined under N_2 and reduced under H_2 at 200 °C for 1 h and 3 h, respectively. See [Supporting Information](#) pages 2–3 for more details.

2.2. Catalyst characterization

The as-synthesized $\text{Pd}_x\text{M}_{100-x}$ NPs were characterized using powder X-ray diffraction (PXRD) to confirm metal alloying and for crystal structure analysis. The NP size and shape were analysed using low-resolution transmission electron microscopy (LR-TEM). Scanning transmission electron microscopy with energy dispersive X-ray spectroscopy (STEM-EDS) was used to measure the NP lattice spacing and analyse the elemental distribution in individual particles. The oxidation state of the NP surface was measured using X-ray photoelectron spectroscopy (XPS). Inductively coupled plasma-optical emission spectroscopy (ICP-OES) was used to determine the bulk elemental composition of the alloy NPs and the percent metal loading of the supported catalysts. The MWCNTs and supported catalysts were characterised using N_2 physisorption for surface area and pore size distribution. Additional details are provided in the [Supporting Information](#) on pages 3–4.

2.3. Catalytic tests

The catalytic activities of the powder catalysts were assessed using an acrylic semi-batch reactor consisting of a cylinder fitted with a magnetic stirrer suspended from the removable top lid, a glass diffuser, a gas outlet port, a sample injection port and a sampling port fitted with a 2 µm stainless steel filter ([Fig. S2](#)). Experiments with the best catalysts were performed in duplicate to validate results, and the associated error was less than 2%. 195 mL of distilled water was initially added to the reactor with 0.125 g L⁻¹ of the selected catalyst, kept in suspension by magnetic stirring at 400 rpm at natural pH (pH 6.0). A flow rate of 50 cm³ min⁻¹ (STP) of hydrogen was fed into the reactor for 15 min to achieve saturation of the liquid phase with hydrogen as well as to promote the reduction of any metal oxide formed over the metallic particles due to contact with air. After this pre-reduction step, a concentrated bromate solution was added to the reactor to achieve an initial concentration of bromate of 200 ppb at a total volume of 200 mL, and the reaction was carried out for 120 min at 25 °C and 1 atm.

The bromate concentration was monitored throughout the reaction by sampling 1 mL aliquots at fixed time intervals and performing analysis with an ion separation column paired with a post-column reaction system and a UV-Vis detector (from Shimadzu). Bromate separation was achieved using a Shim pack SA2 column with a 1 mL min⁻¹ flow rate of a 12 mM NaHCO₃ and 0.6 mM Na₂CO₃ mobile phase. Post-column reaction was carried out with 1.5 M KBr and 1.0 M H₂SO₄ at 0.35 mL min⁻¹ in a first phase, and 1.2 mM NaNO₂ at 0.25 mL min⁻¹ in a second phase, at 40 °C. The post-column reaction allowed conversion of the bromate in solution into tribromide by stepwise reaction. The tribromide was monitored by measuring absorbance at 268 nm and correlated with bromate standards used for calibration, achieving a quantification limit below 1 ppb.

2.4. Computational methods

All density functional theory (DFT) calculations were performed with the Vienna ab initio simulation package (VASP) code [43], using the generalized gradient approximation method with spin polarization. The Perdew-Burke-Ernzerhof functional method was applied to estimate the exchange-correlation energy within a Kohn-Sham system [44]. The interaction between the ionic core and the valence electrons was described by the projector augmented wave method [45] in a plane wave basis with an energy cut-off of 400 eV [46], with the Brillouin zone sampled at the Γ -point. The convergence criteria for the electronic structure and the atomic geometry were set to 10^{-4} and 0.05 eV Å⁻¹, respectively. The Gaussian smearing method with a finite temperature width of 0.05 eV was used to improve convergence of states near the Fermi level. All calculations used a van der Waals-corrected DFT-D3 method with a zero-damping function [47].

The fcc (111) metal surfaces were modelled using a 4×4 slab with

four layers ([Fig. S3](#)). The most stable structure for each of the $\text{Pd}_x\text{Cu}_{100-x}$ and $\text{Pd}_x\text{Ag}_{100-x}$ alloy catalysts was established using basin-hopping calculations with quantum Sutton-Chen potential, with the initial lattice constant for each composition determined by Vegard's law [48–51]. Once the most stable combination and structure for each alloy was achieved, the global minima for each of the $\text{Pd}_x\text{Cu}_{100-x}$ and $\text{Pd}_x\text{Ag}_{100-x}$ alloy structures were optimized in a similar manner. The average binding energy (E_b) of BrO₃⁻ and H from the solution was sampled from a representative number of sites on these surfaces using [Eq. \(1\)](#)

$$E_b = E_{tot} - E_{slab} - E_{ads} \quad (1)$$

where E_{tot} is the total energy of the adsorption system (*i.e.*, the species adsorbed onto the catalyst surface), E_{slab} is the energy of the bare slab and E_{ads} is the energy of the adsorbate in solution. It was assumed that although hydrogen is present as H₂ in the solution, it would dissociatively adsorb to Pd-containing surfaces and thus was treated as atomic hydrogen, H. Solvent effects were introduced using the implicit solvation model in the VASP-sol code [52,53].

3. Results and discussion

3.1. Characterization of microwave synthesized PdAgNPs and PdCuNPs

A series of catalysts composed of either palladium, palladium–silver or palladium–copper nanoparticles was synthesized using a pw-assisted polyol method ([Fig. S1](#)), which were used to assess the impacts of intrinsically alloying Pd with either a semi-noble or non-noble metal for BrO₃⁻ reduction. The molar ratio of the particles was controlled by altering the ratio of precursor salts, with target ratios of 3:1, 1:1 and 1:3 corresponding to $x = 75$, 50 and 25 for each alloy. Monometallic PdNPs were synthesized for use as a control catalyst. The average composition of the particles by various techniques was $x = 76.1$, 53.0 and 27.3 for $\text{Pd}_x\text{Ag}_{100-x}$ NPs and $x = 72.1$, 50.5 and 21.3 for $\text{Pd}_x\text{Cu}_{100-x}$ NPs ([Table S1](#)). Thus, finely controlled compositions of both PdAg and PdCu alloys could be achieved.

Powder X-ray diffraction (PXRD) patterns of both sets of alloyed NPs are presented in [Figs. 1a](#) and [S4](#). The patterns show one set of reflections corresponding to the face-centered cubic (fcc) structure, similar to pure Pd, Ag and Cu. The Bragg reflections of the $\text{Pd}_x\text{Ag}_{100-x}$ NPs were between the standard reflections of Pd ($2\theta_{max} = 40.11^\circ$) and Ag ($2\theta_{max} = 38.11^\circ$), with the shift of the reflections corresponding to the composition of each alloy. For example, the maximum (111) reflection for $\text{Pd}_{50}\text{Ag}_{50}$ NPs was located at $2\theta = 39.04^\circ$ ($\text{Pd}_{50}\text{Ag}_{50}$ NP calculated at $2\theta = 39.11^\circ$). Likewise, for $\text{Pd}_x\text{Cu}_{100-x}$ NPs the Bragg reflections appeared between the standard reflections for Pd and Cu ($2\theta_{max} = 43.30^\circ$). For $\text{Pd}_{50}\text{Cu}_{50}$ NPs, the maximum (111) reflection was located at $2\theta = 41.56^\circ$ ($\text{Pd}_{50}\text{Cu}_{50}$ NP calculated at $2\theta = 41.70^\circ$). The lattice *d*-spacings of the PdAgNPs and PdCuNPs were measured from the PXRD patterns and are shown in [Fig. 1b](#) and [Table S2](#). The measured spacings agree with those calculated by Vegard's Law, further confirming complete alloying for both sets of particles. Low-resolution transmission electron microscopy (LR-TEM) images of the NPs, which are shown in [Fig. 1c](#), reveal that both series of particles adopt a cuboctahedral morphology as expected for fcc nanocrystals [54,55]. However, the two alloys behave very differently under similar synthesis conditions. Despite the presence of PVP, the $\text{Pd}_x\text{Ag}_{100-x}$ NPs tend to agglomerate and form non-uniform particles; the particles with $x = 50$ and 75 were *ca.* 5.2 and 4.4 nm, respectively. When Ag is the major component of the nanoparticle catalyst (*i.e.*, $\text{Pd}_{25}\text{Ag}_{75}$ NPs), the particles grow together into networks of alloyed Pd–Ag. In contrast, $\text{Pd}_x\text{Cu}_{100-x}$ NPs formed well-defined, monodisperse particles with no evidence of agglomeration; the particles had sizes ranging from 3.4 to 4.0 nm. Synthesized monometallic PdNPs were also well-defined cuboctahedra with an average measured size of 4.8 nm ([Fig. S5](#)).

Random alloying of both $\text{Pd}_x\text{Ag}_{100-x}$ NPs and $\text{Pd}_x\text{Cu}_{100-x}$ NPs was

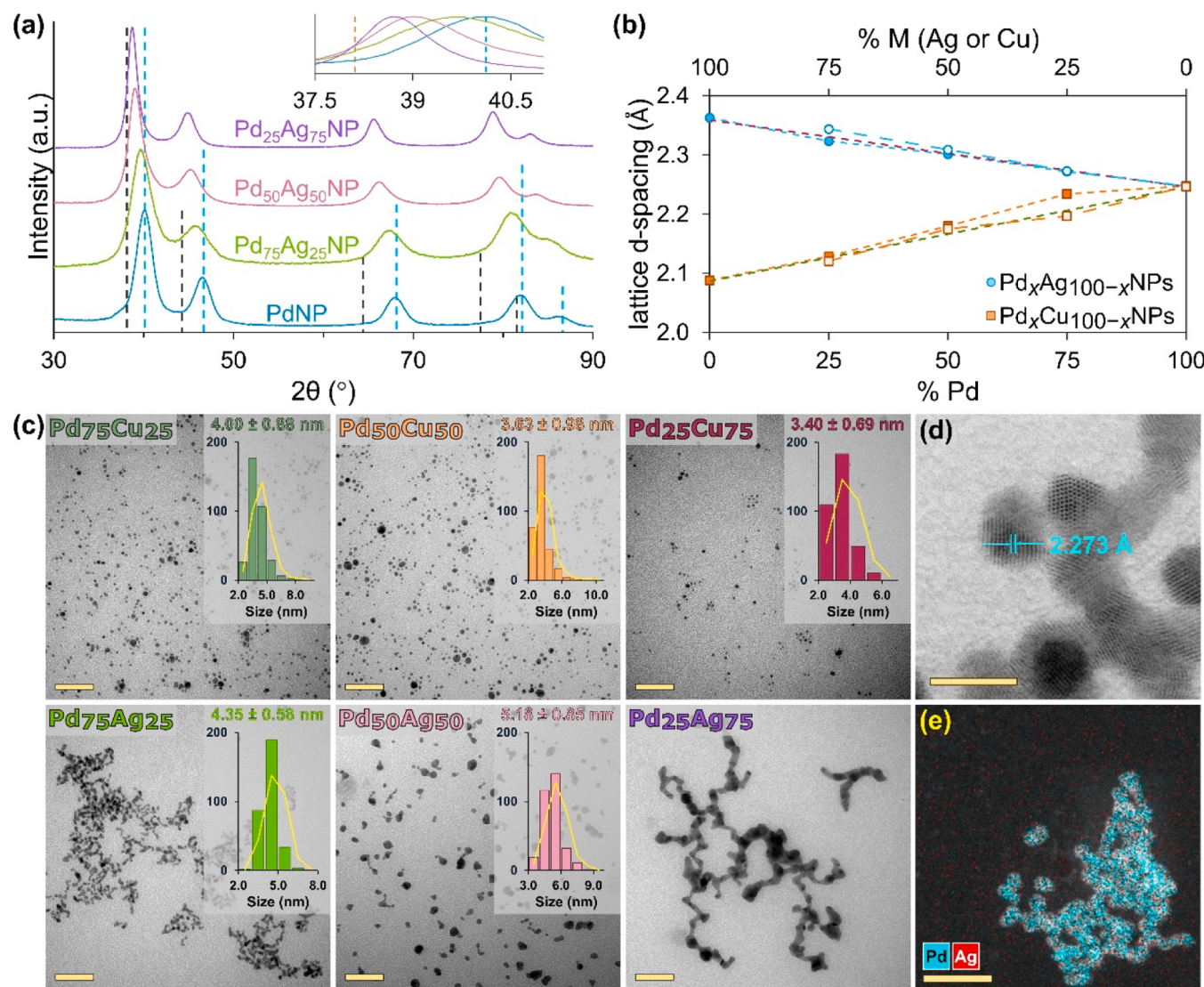


Fig. 1. (a) PXRD patterns of $\text{Pd}_x\text{Ag}_{100-x}$ NPs with expected reflections shown for monometallic Pd (vertical dashed blue lines) and monometallic Ag (vertical dashed grey lines); inset shows an expansion of the (111) peak maxima. (b) Vegard's plot of calculated lattice d -spacings from PXRD (filled) and STEM (empty). Blue circles represent $\text{Pd}_x\text{Ag}_{100-x}$ NPs; orange squares represent $\text{Pd}_x\text{Cu}_{100-x}$ NPs. Dashed lines represent theoretical lattice spacings for PdAg alloys (red) and PdCu alloys (green) calculated with Vegard's Law. (c) Representative LR-TEM images for the three $\text{Pd}_x\text{Ag}_{100-x}$ NPs and $\text{Pd}_x\text{Cu}_{100-x}$ NPs. Insets are histograms with the measured size distribution; scale bars shown are 50 nm. (d) STEM BF image of $\text{Pd}_{75}\text{Ag}_{25}$ NPs showing the measured d -spacing of 2.273 Å corresponding to the {111} planes. Scale bar shown is 5 nm. (e) EDS elemental overlay map of Pd and Ag on $\text{Pd}_{75}\text{Ag}_{25}$ NPs. Scale bar shown is 20 nm.

further confirmed via scanning transmission electron microscopy (STEM) with energy dispersive X-ray spectroscopy (EDS) elemental mapping, shown in Figs. 1d, e and S6–S12. An interplanar distance of 2.273 Å was measured for the $\text{Pd}_{75}\text{Ag}_{25}$ NPs corresponding to the {111} lattice planes of an fcc structure. This spacing closely agrees with that calculated from the powder diffraction pattern (2.272 Å) and the theoretical spacing of 2.274 Å based on Vegard's Law between pure Pd and pure Ag (pure fcc Pd {111} = 2.246 Å; pure fcc Ag {111} = 2.359 Å) [56, 57]. Moreover, the measured lattice spacing increased as the fraction of Pd in the PdAg alloy decreased (2.309 Å and 2.344 Å for $\text{Pd}_{50}\text{Ag}_{50}$ NPs and $\text{Pd}_{25}\text{Ag}_{75}$ NPs, respectively). These results are in good agreement with previous work looking at PdAgNPs [29]. Similarly, an interplanar distance of 2.197 Å was measured for the $\text{Pd}_{75}\text{Cu}_{25}$ NPs, which corresponds to the {111} lattice planes. This spacing closely agrees with that calculated from the diffraction pattern (2.234 Å) and the theoretical spacing of 2.206 Å (pure fcc Cu {111} = 2.087 Å). It should be noted that the metallic Cu d -spacing is smaller than both CuO and Cu₂O (2.533 and 2.458 Å, respectively [58]), and the observed trends in d -spacing match incorporation of Cu, not an oxidized species. EDS elemental mapping

and linescan analysis further confirmed random and homogeneous alloying over the entire composition range of both the PdAg system and the PdCu system, with no structural segregation or core@shell formation (Figs. S7–S12 and Table S1). Overall, the compositions of the PdAgNPs as measured by EDS are in good agreement with the target compositions ($\pm 2\%$). The compositions of the PdCuNPs as measured by EDS display a slight Cu-bias which could be due to both a slight Cu preference for the nanoparticle surface caused by exposure to air during storage, as well as Cu contamination within the STEM-EDS instrument.

X-ray photoelectron spectroscopy (XPS) was used to glean surface specific composition information, and the results are presented in Figs. 2 and S13–S16. Generally, the observed photoelectrons in XPS radiate from the top 5–10 nm of a sample; thus, it could be expected that XPS probes the entirety of small (2–8 nm) nanostructures. However, the added size of the PVP adlayer serves to restrict XPS to surface analysis [59–61]. In addition, the XPS measurements may not reflect the NP catalysts *in situ*, due to the presence of competing oxidizing and reducing species in the catalytic reactor. In general, the elemental composition, as measured by XPS, is in good agreement with

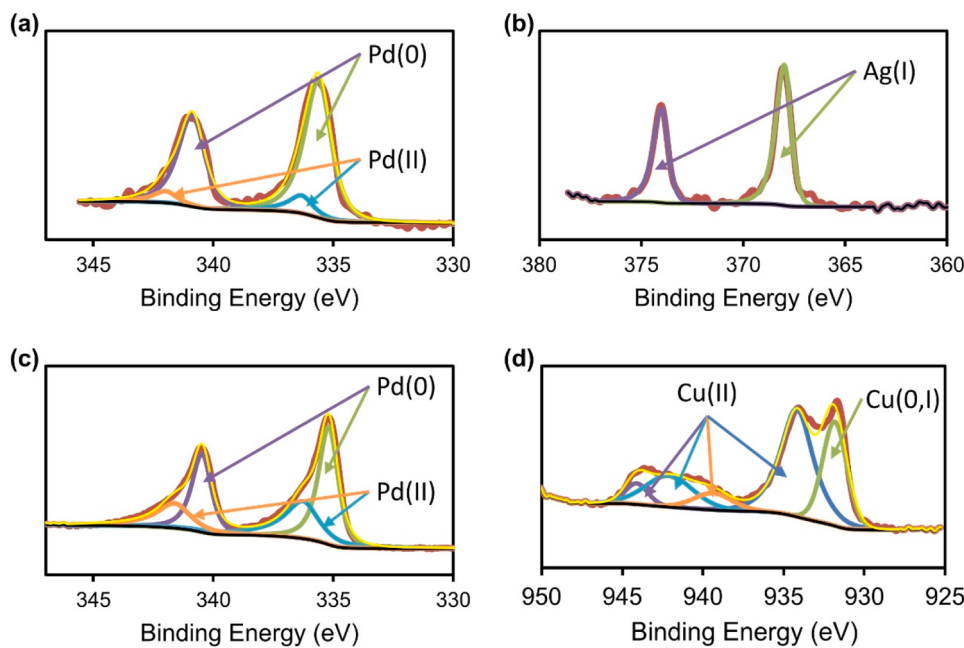


Fig. 2. XPS spectra of the (a) Pd 3d region and (b) Ag 3d region for unsupported Pd₇₅Ag₂₅NPs, and the (c) Pd 3d region and (d) Cu 2p region for unsupported Pd₅₀Cu₅₀NPs.

measurements from ICP-OES and EDS (Table S1). However, a slight Ag- and Cu-bias was observed on the surface of the particles by XPS due to the difference in oxophilicity of the metals, as evidenced by their galvanic potentials ($E^\circ_{\text{Pd}} = 0.92 \text{ V}$, $E^\circ_{\text{Ag}} = 0.80 \text{ V}$ and $E^\circ_{\text{Cu}} = 0.34 \text{ V}$) [62]. Ag and Cu are expected to preferentially migrate to the nanoparticle surface in their native air-exposed state as they are more easily oxidized. XPS was also used to discern the chemical state of the metals in the resulting PdAgNPs and PdCuNPs. Overall, the proportion of Pd(II) to Pd(0) remained relatively constant for the PdAgNPs regardless of the overall composition of the NPs, indicating that the addition of more Ag did not induce a large transfer of electron density from the Pd. The majority of the Pd (82–86%) in the PdAgNPs was present in the metallic Pd(0) state, with binding energies of Pd 3d_{5/2} and 3d_{3/2} at 335.2 and 340.5 eV, respectively (Tables S3 and S4). Additionally, minor peaks were located at 336.6 and 342.1 eV, most likely stemming from PdO formed at the surface of the particles during purification and storage (Figs. 2a, S13 and S14, and Table S4) [63,64]. Similar to our previous study with PdAgNPs [29], the Ag XPS spectra showed only a single doublet corresponding to Ag(I), with binding energies for Ag 3d_{5/2} and 3d_{3/2} at 367.9 and 373.9 eV, respectively (Figs. 2b, S13 and S14, and Table S5) [65–68].

In stark contrast, a much lower fraction of Pd in the PdCuNPs was present in the Pd(0) state (42–62%) with binding energies of Pd 3d_{5/2} and Pd_{3/2} at 335.2 and 340.5 eV, respectively (Figs. 2c, S15 and S16, and Table S4); this can be attributed to the smaller particle sizes of the PdCuNPs which results in a higher fraction of surface Pd atoms which can be oxidized [51,69]. The chemical state of the reactive Pd in the catalytic reactor will be strongly affected by the redox environment, and thus it is not advisable to extract conclusions regarding the influence of Pd species as detected by XPS characterization on the activity of the catalysts. Interestingly, the fraction of oxidized Pd increased as x (the total fraction of Pd in the NP) decreased in contrast to what is expected based on the electronegativities of Pd and Cu (2.2 and 1.9, respectively, on the Pauling Scale). This increase in oxidized Pd could be due to electron density shifting from the Pd to the Cu due to the presence of oxygen binding to surface copper sites. In all three PdCuNP samples, the Cu was primarily present as Cu(OH)₂ based on visual analysis of the shakeup peak shape (Figs. 2d, S15 and S16, and Table S6) [67,70,71]. Comparing the area under the shakeup peak with that under the main Cu

2p peak confirms this; for the Pd₅₀Cu₅₀NPs and Pd₂₅Cu₇₅NPs, ca. 74% of the copper was present as Cu(II), with the rest a mix between Cu(0) and Cu(I). The strong presence of oxidized Cu is most likely due to the oxidation of surface atoms during storage in an ambient atmosphere. Interestingly, the fractions of both metals that are present in an oxidized state increased as the overall fraction of Pd in the PdCuNPs decreased. However, it is anticipated that the presence of oxidized surface atoms will have little impact on the catalytic reduction of BrO₃⁻ as the catalysts are pre-reduced with H₂ gas prior to the reaction, which has been shown to reduce the surface and promote catalytic activity [42].

3.2. Catalytic bromate reduction

To probe the effects of substituting a non- or semi-noble metal for Pd on catalytic bromate reduction, the prepared nanoparticles were deposited on multiwalled carbon nanotubes (MWCNTs) and tested in semi-batch reactors for the hydrogenation of aqueous BrO₃⁻ using H₂ gas as the electron donor (see Experimental Section for details). Prior to use, the elemental composition of the MWCNTs was measured by CNHS + O analysis and was in accordance with the manufacturer's specifications (Table S7). Particles were deposited on MWCNTs; ICP-OES of the prepared catalysts measured actual loadings of 0.4–1.8 wt% total metal (*i.e.*, [Pd + Ag] or [Pd + Cu]; Table S8), and TEM analysis confirmed no change in the NP morphology (Fig. S17).

Bromate reduction versus time for the various Pd_xM_{100-x}NP catalysts are presented in Fig. 3a. All catalysts displayed pseudo-first-order kinetics, from which apparent first-order rate constants were calculated, which are shown in Fig. 3b. The rate constants were then normalized using the total Pd loading of the catalysts, as well as the total metal loading of each catalyst (Figs. 3c, S18a and Table S9); the rate constants were also used to calculate turnover frequencies (TOFs; Fig. S18b) for each catalyst according to the number of active surface sites as measured by H₂ chemisorption (Table S10). The full conversion of bromate into bromide by catalytic reduction has already been thoroughly demonstrated, and thus full bromate transformation was considered in our analysis [19,20,28].

Clear differences in the performances of the catalysts were observed amongst the Pd_xCu_{100-x}NP and Pd_xAg_{100-x}NP catalysts, as well as between the two metal combinations. Interestingly, only one composition

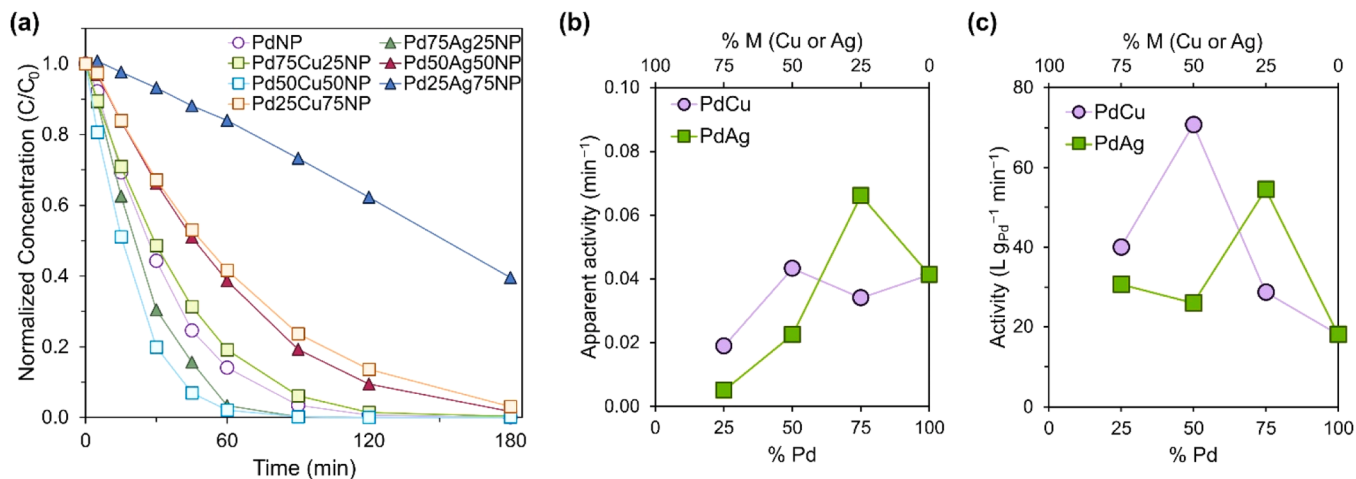
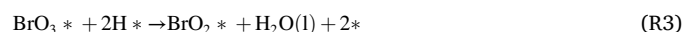


Fig. 3. (a) Dimensionless concentration of BrO_3^- during reduction experiments using MWCNT-supported $\text{Pd}_x\text{M}_{100-x}\text{NP}$ catalysts ($\text{M} = \text{Cu or Ag}$). (b) Calculated apparent pseudo-first order rate constants (in units of per min) for BrO_3^- reduction over $\text{Pd}_x\text{Ag}_{100-x}\text{NP}$ -MWCNTs (green squares) and $\text{Pd}_x\text{Ag}_{100-x}\text{NP}$ -MWCNTs (purple circles). (c) Catalyst activity-per-g Pd (in units of litres per min per g Pd) of MWCNT-supported catalysts as a function of metal composition.

from each metal pair outperformed the monometallic PdNP-MWCNT catalyst when comparing the apparent rate (Fig. 3a: green triangles and blue squares versus purple circles, and 3b). When the rate constant is normalized to the amount of Pd in the catalyst, both alloy series displayed a volcano-shaped relationship with particle composition (Fig. 3c). For the $\text{Pd}_x\text{Ag}_{100-x}\text{NP}$ -MWCNTs, the highest activity was displayed by the $\text{Pd}_{75}\text{Ag}_{25}\text{NP}$ -MWCNT catalyst, with an activity of $54.5 \text{ L g}_{\text{Pd}}^{-1} \text{ min}^{-1}$; for the $\text{Pd}_x\text{Cu}_{100-x}\text{NP}$ -MWCNTs, the $\text{Pd}_{50}\text{Cu}_{50}\text{NP}$ -MWCNT catalyst displayed the highest activity ($70.7 \text{ L g}_{\text{Pd}}^{-1} \text{ min}^{-1}$). Both catalysts displayed significant activity enhancement over the monometallic PdNP-MWCNT ($18.2 \text{ L g}_{\text{Pd}}^{-1} \text{ min}^{-1}$). The trend displayed by the PdAgNP catalysts matches that seen in NO_2^- reduction over PdAgNPs supported on amorphous silica (SiO_2) [29], where reduction activity peaked with just a small (*ca.* 5%) addition of Ag. However, the trend seen in the PdCuNP catalysts differs from that observed when using unsupported PdCuNPs for NO_2^- reduction, where reduction rates increased with decreasing amounts of Cu peaking with $\text{Pd}_{80}\text{Cu}_{20}\text{NPs}$ [31]. All of the tested alloys exhibited improved Pd-normalized BrO_3^- activity compared to the PdNP-MWCNT catalyst (Table S9). Additionally, all catalysts displayed Pd-normalized activity comparative to some of the most active reported catalysts found in the literature (Fig. S19 and Table S11).

3.3. Binding energy on PdAg and PdCu ensembles

Similar to other oxyanion contaminants, such as nitrite, bromate reduction with hydrogen on a noble metal surface is expected to follow a stepwise mechanism of deoxygenation to transform adsorbed BrO_3^- (BrO_3^{*}) to adsorbed bromine (Br^*) which desorbs into solution as the bromine ion (Br^-) [13]. However, unlike nitrite and nitrate, bromate reduction consists of a single pathway to form one product, bromine. To the best of our knowledge, this sequential reduction of BrO_3^- via noble metal catalysts has not previously been investigated using density functional theory studies. Thus, to gain insights into the mechanism responsible for the improved reduction activity of $\text{Pd}_x\text{M}_{100-x}\text{NP}$ catalysts, we used density function theory (DFT) to investigate the sequential pathway of BrO_3^- hydrogenation on a series of close-packed fcc (111) surfaces. The (111) facet was chosen since it has the lowest surface energy for the elements of interest in this study [72]. It is assumed that the source of hydrogen is an adsorbed H atom (H^*) dissociated from H_2 on the catalyst surface. The following elementary steps in the hydrogenation reaction are considered:



where the asterisk (*) denotes a binding site on the metal catalyst surface (Fig. S20). The free energy profile of the reaction is shown in Fig. S21 on a pure Pd surface, $\text{Pd}_x\text{Cu}_{100-x}$ surfaces and $\text{Pd}_x\text{Ag}_{100-x}$ surfaces under standard conditions ($T = 298.15 \text{ K}$). The barriers of each elementary step are not here considered, but this level of thermodynamic analysis has been demonstrated as a good proxy for catalytic activity [73,74]. DFT results show that each step of bromate hydrogenation is exothermic, and thus is expected to occur spontaneously at room temperature conditions. Therefore, it is expected that the binding energy of bromate and atomic H to the catalyst surface (Eqs. R1 and R2) are effective descriptors to estimate the overall reduction activity [29, 51].

On close-packed fcc (111) surfaces, the 3-fold triatomic ensemble is the smallest repeat unit that determines the site-specific activity of a catalyst [75,76]. DFT results demonstrate that BrO_3^- binds through all three oxygens to atop sites within the triatomic ensemble, shown in Figs. 4a and S22, while H preferentially binds at the hollow site of the triatomic ensemble, shown in Fig. S20, similar to the binding geometries of N, C and O on fcc (111) metal surfaces [76–78]. Fig. 4 and Tables S12 and S13 show the binding energies of BrO_3^- and H on the various possible triatomic ensembles (Pd_3 , Pd_2M_1 , Pd_1M_2 , and M_3 , where $\text{M} = \text{Cu or Ag}$) of $\text{Pd}_x\text{Cu}_{100-x}$ and $\text{Pd}_x\text{Ag}_{100-x}$ surfaces ($x = 25, 50, \text{ and } 75$), respectively. The average binding energy for each intermediate alloy composition (represented by the black squares in Fig. 4) is calculated from the histograms of the unique binding sites on the surface. Overall, BrO_3^- binding on both $\text{Pd}_x\text{Cu}_{100-x}$ and $\text{Pd}_x\text{Ag}_{100-x}$ is much stronger than H binding. Additionally, the binding energies for BrO_3^- and H on the different ensemble sites are in relative agreement on a given $\text{Pd}_x\text{Cu}_{100-x}$ surface, so all ensemble sites for a given $\text{Pd}_x\text{Cu}_{100-x}$ composition can be examined as a single entity. On PdCu surfaces, BrO_3^- binding displays a volcano-shape dependence on alloy composition (Fig. 4a), with BrO_3^- binding most strongly (*i.e.*, most negatively) on a $\text{Pd}_{50}\text{Cu}_{50}$ surface with an average energy of -1.56 eV . As the amount of Pd in the alloy is increased, BrO_3^- binding becomes weaker (*i.e.*, more positive); BrO_3^-

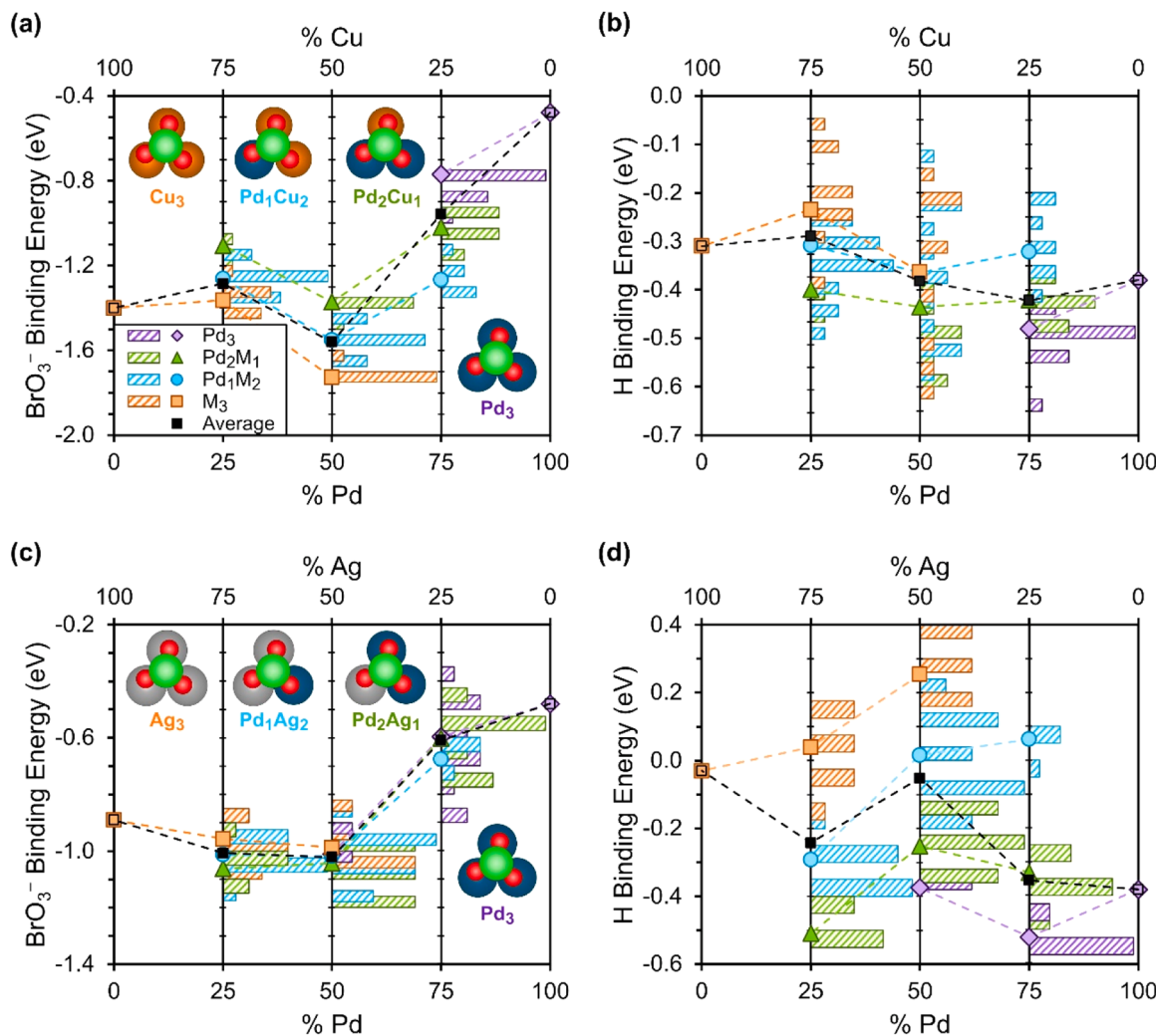


Fig. 4. Decomposition of the average BrO₃⁻ and H binding energies onto the specific surface ensemble sites as determined by the number of Pd versus M atoms at the binding site and the overall composition of the catalyst: (a) BrO₃⁻ binding on Pd_xCu_{100-x} catalysts, (b) H binding on Pd_xCu_{100-x} catalysts, (c) BrO₃⁻ binding on Pd_xAg_{100-x} catalysts and (d) H binding on Pd_xAg_{100-x} catalysts. The horizontal histogram bars indicate the frequency of different binding energies at the three compositions, and the solid symbols indicate the average binding energy per specific site. The black squares indicate the overall average BrO₃⁻ binding energy for each composition. The insets show the representative adsorption geometry of BrO₃⁻ on each possible triatomic ensembles: Pd₃, Pd₂Cu₁, Pd₁Cu₂, Cu₃, Pd₂Ag₁, Pd₁Ag₂ and Ag₃; blue atoms are Pd, orange are Cu, grey are Ag, green are Br and red are O.

binds most weakly to a pure Pd surface with an energy of -0.48 eV. When the amount of Cu in the alloy is increased to 75% (Pd₂₅Cu₇₅), the binding energy weakens before becoming stronger on pure Cu (-1.40 eV). However, pure Cu is not expected to display reduction activity as it is unable to dissociate H₂ to form atomic H. Interestingly, atomic H binds most strongly to a Pd₇₅Cu₂₅ surface (-0.42 eV), slightly stronger than H binding on a pure Pd surface (-0.38 eV). H binding becomes weaker (more positive) as the concentration of Cu increases so that H binds more strongly to a Pd₇₅Cu₂₅ surface than a Pd₅₀Cu₅₀ surface than a Pd₂₅Cu₇₅ surface (Fig. 4b). However, the difference in H binding energies on a Pd₇₅Cu₂₅ surface versus a Pd₅₀Cu₅₀ surface versus a Pd₂₅Cu₇₅ is much smaller than the difference in BrO₃⁻ binding energies on these surfaces ($\Delta E_{b,H} = 0.04$ and 0.09 eV versus $\Delta E_{b,bromate} = 0.60$ and 0.28 eV), so the BrO₃⁻ binding energy is anticipated to be a better descriptor of catalyst activity. Importantly, the trends for both BrO₃⁻ and H binding are in excellent agreement with our experimental observations (Fig. 3) that the Pd₅₀Cu₅₀NP catalyst is the most active for BrO₃⁻ hydrogenation.

The BrO₃⁻ binding energy also displays a volcano-shaped composition dependence on PdAg surfaces (Fig. 4c), and the BrO₃⁻ binding energies on the different ensembles of each Pd_xAg_{100-x} surface are in close

agreement. Bromate binding is weakest (most positive) on a pure Pd surface (-0.48 eV) and becomes stronger (more negative) as the amount of Ag is increased, peaking on a Pd₅₀Ag₅₀ surface at -1.02 eV. As the amount of Ag continues to increase to Pd₂₅Ag₇₅ and then pure Ag, the BrO₃⁻ binding energy weakens slightly to -1.01 eV on Pd₂₅Ag₇₅ and -0.89 eV on Ag. However, like pure Cu, pure Ag is not expected to be active for hydrogenation as it cannot dissociate H₂. Interestingly, this trend in BrO₃⁻ binding strength does not agree with our experimental results, which saw the highest activity on a Pd₇₅Ag₂₅NP catalyst. For hydrogen, binding is strongest (most negative) on a pure Pd surface (-0.38 eV; Fig. 4d). When a small amount of Ag is added (Pd₇₅Ag₂₅), the binding energy weakens slightly to -0.35 eV. When the Ag is further increased to Pd₅₀Ag₅₀, the H binding energy significantly weakens to -0.05 eV. Further addition of Ag slightly increases the binding strength of H on a Pd₂₅Ag₇₅ surface (-0.24 eV); H binding on a pure Ag is much weaker than on Pd-containing surfaces (-0.03 eV). The overall difference in H binding energy on a Pd₇₅Ag₂₅ surface versus a Pd₅₀Ag₅₀ surface is much closer to the energy difference in BrO₃⁻ binding on these surfaces ($\Delta E_{b,H} = 0.30$ versus $\Delta E_{b,bromate} = 0.41$ eV), indicating that H binding plays a larger role in determining activity on a Pd_xAg_{100-x} catalyst than on a Pd_xCu_{100-x} catalyst.

To further probe the role of BrO_3^- and H binding on BrO_3^- reduction activity, it is important to also consider BrO_3^- and H binding at the different ensembles (Fig. 4). The H binding energy on Pd_3 sites decreases as the Ag content increases from 25% to 50% (-0.52 eV versus -0.38 eV, respectively), while the BrO_3^- binding energy on Pd_3 sites increases (-0.60 eV versus -1.01 eV). The H binding energy on Pd_2Ag_1 sites has a similar trend (-0.33 eV versus -0.25), but the BrO_3^- binding energy at Pd_2Ag_1 sites again increases as the amount of Ag increases (-0.60 eV versus -1.04 eV). Interestingly, the H binding energy at Pd_1Ag_2 sites on a $\text{Pd}_{75}\text{Ag}_{25}$ surface is energetically unfavourable (0.06 eV), meaning that these sites would be occupied by adsorbed Br-species. The H binding energy at Pd_1Ag_2 sites on a $\text{Pd}_{50}\text{Ag}_{50}$ surface (0.02 eV) is also unfavourable. However, the BrO_3^- binding energy on the Pd_1Ag_2 sites for both these compositions is strong (-0.68 eV and -1.02 eV). Our calculations show that pure silver sites (Ag_3) are unlikely to form on a $\text{Pd}_{75}\text{Ag}_{25}$ surface, and H binding on Ag_3 sites on a $\text{Pd}_{50}\text{Ag}_{50}$ surface is highly unfavourable (0.25 eV), whereas the BrO_3^- binding energy is strong (-0.99 eV). Thus, BrO_3^- is more likely to bind to the Pd_1Ag_2 or Ag_3 sites when introduced to a H saturated $\text{Pd}_{75}\text{Ag}_{25}$ or $\text{Pd}_{50}\text{Ag}_{50}$ surface, such as that present in these experiments, because the Pd_3 and Pd_2Ag_1 sites will be strongly occupied by H. With the assumption that both Pd and Ag are randomly distributed in the particles, which is in good agreement with elemental analysis from XPS (see Table S1), a Pd-rich composition is likely to have a higher ratio of Pd_3 and Pd_2Ag_1 sites, thus creating more favourable conditions for H to react with adsorbed Br-species. We posit that the trade-off between the overall strong BrO_3^- binding and the more favourable H binding on these Pd-rich sites of the $\text{Pd}_{75}\text{Ag}_{25}$ surface results in an increased activity for BrO_3^- hydrogenation, as demonstrated by our experimental results that show the $\text{Pd}_{75}\text{Ag}_{25}$ NP is the most active PdAg alloy composition for BrO_3^- reduction.

As far as we are aware, our work presents the first attempt to combine both experiment and theory to mechanistically interpret BrO_3^- hydrogenation over Pd-based alloy catalysts. Our combined experimental and theoretical results suggest that enhancing bromate reduction activity is achieved with alloy systems through a combination of electronic and ensemble effects, though, the extent to which each of these effects dominates is dependent on the metal combination. In the PdCu system, electronic effects tend to dictate overall binding energies for both BrO_3^- and H which controls overall reactivity; in the PdAg system, local ensemble effects control the binding of either BrO_3^- or H onto the catalyst surface, and optimization of these sites leads to improved catalytic activity. These findings are in relatively good agreement with the XPS results of the as-synthesized NPs used in this study. For example, the

proportion of Pd(II) in the PdCuNPs increased as x (the amount of Pd in the NP) decreased indicating charge transfer from the Pd to the Cu. In the case of the PdAgNPs, the proportion of Pd(II) to Pd(0) did not change with overall NP composition, which agrees with the DFT derived conclusion that ensemble effects, not charge transfer, was responsible for the increased catalytic activity for bromate reduction. Despite this agreement, it should be noted that the XPS of the unsupported nanoparticles may not be indicative of the catalysts during the reactor due to the presence of oxidizing and reducing species in the reactor.

3.4. Comparison of nanoparticle catalysts with traditional catalysts

To link the insights gleaned from the nanoparticle catalysts to industrially relevant materials, we prepared catalysts via incipient wetness impregnation with analogous compositions (*i.e.*, PdAg-IW-MWCNT, PdCu-IW-MWCNT and Pd-IW-MWCNT) to the highest performing alloys ($\text{Pd}_{75}\text{Ag}_{25}$ NP-MWCNT and $\text{Pd}_{50}\text{Cu}_{50}$ NP-MWCNT) and monometallic Pd. The activity of monometallic non-noble metals has been extensively studied for catalytic bromate reduction and found to be insignificant compared with that of noble metals, regardless of the support in use [20,28]. Results are shown in Fig. 5 and Table S9. Again, all catalysts displayed pseudo-first order kinetics (Fig. 5a) from which apparent first-order rate constants and TOFs were calculated (Table S9). Again, we considered the loss of bromate to be equivalent to the full conversion of bromate into bromide by catalytic reduction based on previous studies [19,20,28]. Interestingly, the apparent first-order rate constants for the incipient wetness catalysts do not follow a similar trend to that of the NP-MWCNT catalysts; while PdCu-IW-MWCNT is the most active catalyst (0.1209 min^{-1}), Pd-IW-MWCNT slightly outperforms the PdAg-IW-MWCNT catalyst (0.0883 min^{-1} vs. 0.0840 min^{-1} , respectively). However, when the activity is normalized to the mass of Pd in the catalyst or converted to TOFs, the trend matches that of the NP-MWCNT catalysts (Fig. 5b). The PdCu-IW-MWCNT catalyst remains the most active ($87.1 \text{ L g}_{\text{Pd}}^{-1} \text{ min}^{-1}$; TOF = 11.9 h^{-1}), followed by the PdAg-IW-MWCNT ($44.7 \text{ L g}_{\text{Pd}}^{-1} \text{ min}^{-1}$; TOF = 7.2 h^{-1}) and then the Pd-IW-MWCNT catalyst ($37.6 \text{ L g}_{\text{Pd}}^{-1} \text{ min}^{-1}$; TOF = 2.2 h^{-1}). Characterization of the incipient wetness catalysts via STEM-EDS reveals that the catalysts prepared by this method also formed alloys of PdAg and PdCu, respectively (Figs. S23 and S24), indicating that the two metals form an alloy structure during incipient wetness deposition. This is in agreement with earlier studies that have found alloy phases are present in catalysts synthesized by co-incipient wetness deposition [42,79,80].

The incipient wetness catalysts slightly outperform their analogous

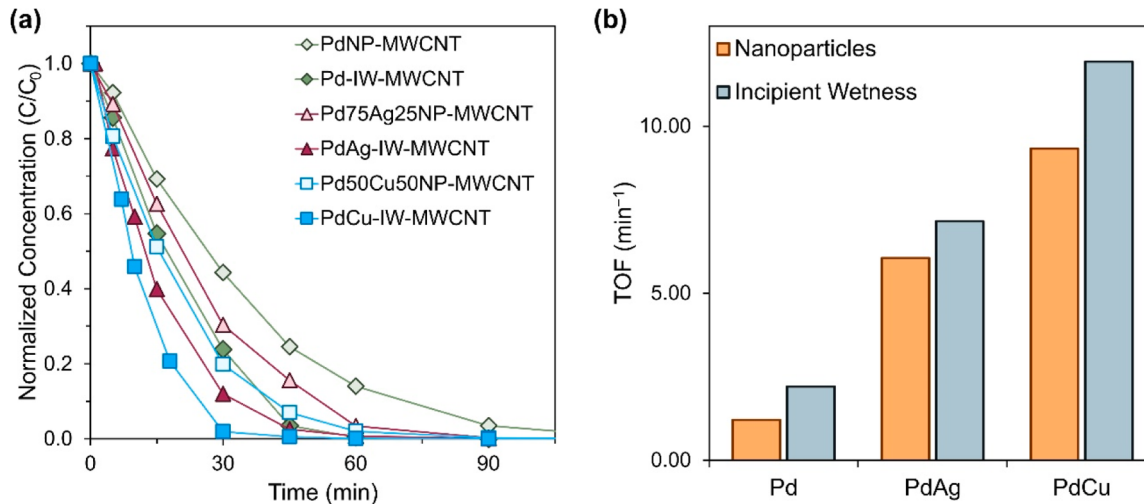


Fig. 5. (a) Dimensionless concentration of BrO_3^- during reduction experiments using PdNP-MWCNTs (empty green diamonds), $\text{Pd}_{75}\text{Ag}_{25}$ NP-MWCNTs (empty red triangles) and $\text{Pd}_{50}\text{Cu}_{50}$ NP-MWCNTs (empty blue squares) and analogous incipient wetness catalysts (corresponding filled shapes). (b) Comparison of the calculated TOFs in units of BrO_3^- ions per Pd surface site per min for analogous NP and incipient wetness catalysts.

nano particle catalysts when the apparent activity is normalized to TOFs; however, this difference is small (within 25%). This agrees with the H₂ uptake data from chemisorption experiments (Table S10). In all cases, the catalysts synthesized via incipient wetness display a slightly higher uptake of H₂ than the NP catalyst. Thus, it seems like the small disparity in TOFs could be attributed to the different synthesis methods. When synthesizing the nanoparticle catalysts, a capping agent (PVP) is used to control the growth of the particles and to prevent agglomeration. While the majority of the PVP is washed off before the particles are deposited onto the MWCNTs, inevitably some remains on the surface of the particles which could reduce access to active surface sites needed for BrO₃⁻ reduction. However, PVP is not used in incipient wetness, and thus this issue is non-existent. Additionally, it is possible that some metal-support interaction is induced during incipient wetness impregnation that is not present when nanoparticles are deposited on the MWCNTs due to the high temperatures used to calcine and reduce the metals during incipient wetness. Similarly, analysis of bimetallic catalysts synthesized using incipient wetness does not always display complete alloying of the metals, meaning that there might be monometallic phases along with alloy phases of various ratios. Moreover, as extensively reported, the pH_{pzc} of the as-received MWCNT supports is approximately 7.0 [81]. As this value is above that of the bromate solution pH, a positive surface charge is formed which benefits interactions with the bromate anions in solution [22]. However, the small differences in TOF measured here, combined with the low weight loadings of the catalyst, mean that elucidating a material reason for these differences is at best extremely challenging and not recommend unless greater TOF differences are observed in future studies.

It is important to note that the applicability of bimetallic Pd-based catalysts (and even monometallic Pd-based catalysts) is dependent on their long-term stability and reusability, as well as their performance in real waters. In this current work, our focus was to investigate the mechanisms by which bimetallic PdCu and PdAg catalysts improve bromate reduction activity and not to study the longevity of these materials. Thus, we chose to use our materials once and to perform reduction experiments in deionized water. However, previous studies from our groups demonstrated that similar catalysts are stable and yield high bromate conversion over an extended time period or with multiple uses, with only a slight degree of activity loss. Additionally, these studies show that metal leaching is not a concern for these materials [20,28,82]. Further, previous studies have shown that bromate reduction in real waters is inhibited by the presence of ions that can competitively bind to the catalyst surface forming mineral deposits which effectively poison the catalyst [82]. Using intelligent design to identify optimal bimetallic alloys, like that shown in this work, may present a means to not only improve catalyst activity, but to also create catalysts that are more resilient in real waters. However, further studies are needed to assess the viability of using model nanoparticle catalysts paired with DFT in addressing these questions.

4. Conclusions

In this present work, we demonstrated that substituting a semi- or non-noble metal (*i.e.*, Ag or Cu, respectively) for Pd is a feasible strategy to improve the activity of catalytic BrO₃⁻ reduction at environmentally relevant drinking water concentrations (10's–100's µg-BrO₃⁻ L⁻¹). Catalysts based on Pd₇₅Ag₂₅NPs and Pd₅₀Cu₅₀NPs supported on MWCNTs showed significant improvement in activity when compared to a monometallic PdNP-MWCNT catalyst. Our experimental and theoretical results demonstrate that these PdAgNP and PdCuNP catalysts exploit intrinsic electronic effects and local ensemble effects which create energetically more favourable BrO₃⁻ and H binding conditions than on pure PdNP catalysts. These conditions engender faster reaction rates and thus higher catalyst activity. Further, we have demonstrated that the insights gained from the alloy NP catalysts are directly transferrable to catalysts synthesized by traditional methods, such as

incipient wetness deposition, which is shown to also create alloy catalysts. The assessment here, performed at realistic conditions (µg L⁻¹), demonstrates that the preparation and selection of optimized bimetallic catalysts using model nanoparticle-based materials has the potential to intelligently direct catalyst synthesis for the industrial scale.

CRedit authorship contribution statement

João Restivo: Writing – review & editing, Writing – original draft, Visualization, Methodology, Conceptualization. **Graeme Henkelman:** Writing – review & editing, Supervision, Funding acquisition. **Jacob P. Troutman:** Writing – review & editing, Writing – original draft, Visualization, Methodology, Investigation, Conceptualization. **Simon M. Humphrey:** Writing – review & editing, Supervision, Funding acquisition. **Manuel F. R. Pereira:** Writing – review & editing, Supervision, Funding acquisition. **Carla A. Orge:** Writing – review & editing, Supervision, Funding acquisition, Conceptualization. **José R.M. Barbosa:** Investigation. **Carolina Vigil-Hernandez:** Investigation. **João M. B. Costa:** Investigation. **Carolyn E. Brady:** Investigation. **Zahra Bajalan:** Writing – original draft, Methodology, Investigation. **Olívia Salomé Soares:** Writing – review & editing, Supervision, Funding acquisition, Conceptualization. **Hyunwoo Ha:** Writing – original draft, Methodology, Investigation. **Charles J. Werth:** Writing – review & editing, Supervision, Funding acquisition, Conceptualization.

Declaration of Competing Interest

The authors declare that they have no known competing financial interests or personal relationships that could have appeared to influence the work reported in this paper.

Data availability

Data will be made available on request.

Acknowledgements

The authors thank Michelle Mikesh (UT Austin; LR-TEM), Dr. Hugo Celio (UT Austin; XPS), Dr. Karalee Jarvis (UT Austin; STEM-EDS) and Dr. Vincent Lynch (PXRD) for assistance with catalyst characterization. Funding for this work was provided by NanoCatRed (NORTE-01-0247-FEDER-045925) (ERDF – COMPETE 2020, – NORTE 2020 and – FCT under UT Austin Portugal), the National Science Foundation under Grant No. CBET-1922504 and the Welch Foundation ((F-1738 (S.M.H.) & F -1841 (G.H.))). This work was also financially supported by): LSREL-CM, UIDB/50020/2020 (DOI: [10.54499/UIDB/50020/2020](https://doi.org/10.54499/UIDB/50020/2020)) and UIDP/50020/2020 (DOI: [10.54499/UIDP/50020/2020](https://doi.org/10.54499/UIDP/50020/2020)); and ALICE, LA/P/0045/2020 (DOI: [10.54499/LA/P/0045/2020](https://doi.org/10.54499/LA/P/0045/2020)), funded by national funds through FCT/MCTES (PIDDAC). CAO acknowledges FCT funding under DL57/2016 Transitory Norm Programme. OSGPS acknowledges FCT funding under the Scientific Employment Stimulus - Institutional Call CECINST/00049/2018 (DOI 10.54499/CECINST/00049/2018/CP1524/CT0008). Computational resources were provided by the Extreme Science and Engineering Discovery Environment (XSEDE), the Advanced Cyberinfrastructure Coordination Ecosystem: Services and Support (ACCESS) and the Texas Advanced Computing Center (TACC) under the allocation CHE190010 – Modelling Materials for Energy Conversion and Storage Over Experimental Timescales.

Appendix A. Supporting information

Supplementary data associated with this article can be found in the online version at [doi:10.1016/j.apcata.2024.119654](https://doi.org/10.1016/j.apcata.2024.119654).

References

- [1] T.P. Bonacquisti, A drinking water utility's perspective on bromide, bromate, and ozonation, *Toxicology* 221 (2006) 145–148, <https://doi.org/10.1016/j.tox.2006.02.010>.
- [2] W.H. Glaze, Drinking-water treatment with ozone, *Environ. Sci. Technol.* 21 (1987) 224–230, <https://doi.org/10.1021/es00157a001>.
- [3] B. Langlais, D.A. Reckhow, D.R. Brink, eds., *Ozone in Water Treatment: Application and Engineering*, CRC Press/Taylor & Francis, Boca Raton, FL, 1991.
- [4] B.N. Jahan, L. Li, K.R. Pagilla, Fate and reduction of bromate formed in advanced water treatment ozonation systems: A critical review, *Chemosphere* 266 (2021) 128964, <https://doi.org/10.1016/j.chemosphere.2020.128964>.
- [5] F. Soltermann, C. Abegglen, C. Götz, U. Von Gunten, Bromide Sources and Loads in Swiss Surface Waters and Their Relevance for Bromate Formation during Wastewater Ozonation, *Environ. Sci. Technol.* 50 (2016) 9825–9834, <https://doi.org/10.1021/acs.est.6b01142>.
- [6] WHO, *Guidelines for Drinking-Water Quality, 4th ed.*, World Health Organization,, 2017.
- [7] F. Soltermann, C. Abegglen, M. Tschui, S. Stahel, U. von Gunten, Options and limitations for bromate control during ozonation of wastewater, *Water Res* 116 (2017) 76–85, <https://doi.org/10.1016/j.watres.2017.02.026>.
- [8] J.A. Wiśniewski, M. Kabsch-Korbutowicz, Bromate removal in the ion-exchange process, *Desalination* 261 (2010) 197–201, <https://doi.org/10.1016/j.desal.2010.03.029>.
- [9] Y.Q. Zhang, Q.P. Wu, J.M. Zhang, X.H. Yang, Removal of bromide and bromate from drinking water using granular activated carbon, *J. Water Health* 13 (2015) 73–78, <https://doi.org/10.2166/wh.2014.084>.
- [10] T. Skorjanc, D. Shetty, F. Gárdara, L. Ali, J. Raya, G. Das, M.A. Olson, A. Trabolsi, Remarkably efficient removal of toxic bromate from drinking water with a porphyrin-viologen covalent organic framework, *Chem. Sci.* 11 (2020) 845–850, <https://doi.org/10.1039/c9sc04663a>.
- [11] S. Gyarakis, E. Diamadopoulos, Formation and reverse osmosis removal of bromate ions during ozonation of groundwater in coastal areas, *Sep. Sci. Technol.* 42 (2007) 1465–1476, <https://doi.org/10.1080/01496390701290011>.
- [12] M. Moslemi, S.H. Davies, S.J. Masten, Rejection of bromide and bromate ions by a ceramic membrane, *Environ. Eng. Sci.* 29 (2012) 1092–1096, <https://doi.org/10.1089/ees.2012.0086>.
- [13] B.P. Chaplin, M. Reinhard, W.F. Schneider, C. Schüth, J.R. Shapley, T. J. Strathmann, C.J. Werth, Critical review of Pd-based catalytic treatment of priority contaminants in water, *Environ. Sci. Technol.* 46 (2012) 3655–3670, <https://doi.org/10.1021/es204087q>.
- [14] X. Lv, D. Wang, W. Iqbal, B. Yang, Y. Mao, Microbial reduction of bromate: current status and prospects, *Biodegradation* 30 (2019) 365–374, <https://doi.org/10.1007/s10532-019-09882-x>.
- [15] D.F.S. Morais, R.A.R. Boaventura, F.C. Moreira, V.J.P. Vilar, Bromate removal from water intended for human consumption by heterogeneous photocatalysis: Effect of major dissolved water constituents, *Chemosphere* 263 (2021) 128111, <https://doi.org/10.1016/j.chemosphere.2020.128111>.
- [16] Z. Wu, Y. Tang, X. Yuan, Z. Qiang, Reduction of bromate by zero valent iron (ZVI) enhances formation of brominated disinfection by-products during chlorination, *Chemosphere* 268 (2021) 129340, <https://doi.org/10.1016/j.chemosphere.2020.129340>.
- [17] F. Yao, Q. Yang, J. Sun, F. Chen, Y. Zhong, H. Yin, L. He, Z. Tao, Z. Pi, D. Wang, X. Li, Electrochemical reduction of bromate using noble metal-free nanoscale zero-valent iron immobilized activated carbon fiber electrode, *Chem. Eng. J.* 389 (2020) 123588, <https://doi.org/10.1016/j.cej.2019.123588>.
- [18] J. Qiao, L. Feng, H. Dong, Z. Zhao, X. Guan, Overlooked Role of Sulfur-Centered Radicals during Bromate Reduction by Sulfito, *Environ. Sci. Technol.* 53 (2019) 10320–10328, <https://doi.org/10.1021/acs.est.9b01783>.
- [19] J. Restivo, O.S.G.P. Soares, J.J.M. Órfão, M.F.R. Pereira, Metal assessment for the catalytic reduction of bromate in water under hydrogen, *Chem. Eng. J.* 263 (2015) 119–126, <https://doi.org/10.1016/j.cej.2014.11.052>.
- [20] J. Restivo, O.S.G.P. Soares, J.J.M. Órfão, M.F.R. Pereira, Catalytic reduction of bromate over monometallic catalysts on different powder and structured supports, *Chem. Eng. J.* 309 (2017) 197–205, <https://doi.org/10.1016/j.cej.2016.10.025>.
- [21] C.M.A.S. Freitas, O.S.G.P. Soares, J.J.M. Órfão, A.M. Fonseca, M.F.R. Pereira, I. C. Neves, Highly efficient reduction of bromate to bromide over mono and bimetallic ZSM5 catalysts, *Green. Chem.* 17 (2015) 4247–4254, <https://doi.org/10.1039/c5gc0077a>.
- [22] O.S.G.P. Soares, P.S.F. Ramalho, A. Fernandes, J.J.M. Órfão, M.F.R. Pereira, Catalytic bromate reduction in water: Influence of carbon support, *J. Environ. Chem. Eng.* 7 (2019) 103015, <https://doi.org/10.1016/j.jece.2019.103015>.
- [23] J.L. Cerrillo, A.E. Palomares, A review on the catalytic hydrogenation of bromate in water phase, *Catalysts* 11 (2021) 1–18, <https://doi.org/10.3390/catal11030365>.
- [24] R.P. Pandey, K. Rasool, P.A. Rasheed, K.A. Mahmoud, Reductive Sequestration of Toxic Bromate from Drinking Water using Lamellar Two-Dimensional Ti3C2TX (MXene), *ACS Sustain. Chem. Eng.* 6 (2018) 7910–7917, <https://doi.org/10.1021/acssuschemeng.8b01147>.
- [25] D.D. Tuan, H. Yang, N.N. Huy, E. Kwon, T.C. Khiem, S. You, J. Lee, K.Y.A. Lin, Enhanced reduction of bromate in water by 2-dimensional porous Co3O4 via catalytic hydrogenation, *J. Environ. Chem. Eng.* 9 (2021) 105809, <https://doi.org/10.1016/j.jece.2021.105809>.
- [26] B.C. Li, H. Yang, E. Kwon, D. Dinh Tuan, T. Cong Khiem, G. Lisak, B. Xuan Thanh, F. Ghanbari, K.Y.A. Lin, Catalytic reduction of bromate by Co-embedded N-doped carbon as a magnetic Non-Noble metal hydrogenation catalyst, *Sep. Purif. Technol.* 277 (2021) 119320, <https://doi.org/10.1016/j.seppur.2021.119320>.
- [27] Y. Huang, M. Luo, S. Li, D. Xia, Z. Tang, S. Hu, S. Ye, M. Sun, C. He, D. Shu, Efficient catalytic activity and bromate minimization over lattice oxygen-rich MnOOH nanorods in catalytic ozonation of bromide-containing organic pollutants: Lattice oxygen-directed redox cycle and bromate reduction, *J. Hazard. Mater.* 410 (2021) 124545, <https://doi.org/10.1016/j.jhazmat.2020.124545>.
- [28] J. Restivo, O.S.G.P. Soares, J.J.M. Órfão, M.F.R. Pereira, Bimetallic activated carbon supported catalysts for the hydrogen reduction of bromate in water, *Catal. Today* 249 (2015) 213–219, <https://doi.org/10.1016/j.cattod.2014.10.048>.
- [29] J.P. Troutman, H. Li, A.M. Haddix, B.A. Kienzle, G. Henkelman, S.M. Humphrey, C. J. Werth, PdAg Alloy Nanocatalysts: Toward Economically Viable Nitrite Reduction in Drinking Water, *ACS Catal.* 10 (2020) 7979–7989, <https://doi.org/10.1021/acscatal.0c01538>.
- [30] S. Seraj, P. Kunal, H. Li, G. Henkelman, S.M. Humphrey, C.J. Werth, PdAu Alloy Nanoparticle Catalysts: Effective Candidates for Nitrite Reduction in Water, *ACS Catal.* 7 (2017) 3268–3276, <https://doi.org/10.1021/acscatal.6b03647>.
- [31] K.A. Guy, H. Xu, J.C. Yang, C.J. Werth, J.R. Shapley, Catalytic nitrate and nitrite reduction with Pd–Cu/PVP colloids in water: Composition, structure, and reactivity correlations, *J. Phys. Chem. C* 113 (2009) 8177–8185, <https://doi.org/10.1021/jp810049y>.
- [32] Y. Gao, W. Sun, W. Yang, Q. Li, Creation of Pd/Al2O3 catalyst by a spray process for fixed bed reactors and its effective removal of aqueous bromate, *Sci. Rep.* 7 (2017) 1–11, <https://doi.org/10.1038/srep41797>.
- [33] M.B. Navas, H.P. Bideberripe, C.I. Cabello, D. Gazzoli, M.L. Casella, M. A. Jaworski, Use of PdCu catalysts supported on zirconia-ceria based supports for the elimination of oxyanions present in water, *Catal. Today* 372 (2021) 154–163, <https://doi.org/10.1016/j.cattod.2020.08.012>.
- [34] P. Zhang, F. Jiang, H. Chen, Enhanced catalytic hydrogenation of aqueous bromate over Pd/mesoporous carbon nitride, *Chem. Eng. J.* 234 (2013) 195–202, <https://doi.org/10.1016/j.cej.2013.08.111>.
- [35] N. Dahal, S. García, J. Zhou, S.M. Humphrey, Beneficial Effects of Microwave-Assisted Heating versus Conventional Heating in Noble Metal Nanoparticle Synthesis, *ACS Nano* 6 (2012) 9433–9446, <https://doi.org/10.1021/nm3038918>.
- [36] S. Garcia, L. Zhang, G.W. Piburn, G. Henkelman, S.M. Humphrey, Microwave synthesis of classically immiscible rhodium-silver and rhodium-gold alloy nanoparticles: highly active hydrogenation catalysts, *ACS Nano* 8 (2014) 11512–11521, <https://doi.org/10.1021/nn504746u>.
- [37] D.B. Thakur, R.M. Tiggelaar, Y. Weber, J.G.E. Gardeniers, L. Lefferts, K. Seshan, Ruthenium catalyst on carbon nanofiber support layers for use in silicon-based structured microreactors. Part II: Catalytic reduction of bromate contaminants in aqueous phase, *Appl. Catal. B* 102 (2011) 243–250, <https://doi.org/10.1016/j.apcatb.2010.12.004>.
- [38] P. Kunal, H. Li, B.L. Dewing, L. Zhang, K. Jarvis, G. Henkelman, S.M. Humphrey, Microwave-Assisted Synthesis of Pd x Au $100-x$ Alloy Nanoparticles: A Combined Experimental and Theoretical Assessment of Synthetic and Compositional Effects upon Catalytic Reactivity, *ACS Catal.* 6 (2016) 4882–4893, <https://doi.org/10.1021/acscatal.6b01014>.
- [39] P. Kunal, E.J. Roberts, C.T. Riche, K. Jarvis, N. Malmstadt, R.L. Brutchey, S. M. Humphrey, Continuous Flow Synthesis of Rh and RhAg Alloy Nanoparticle Catalysts Enables Scalable Production and Improved Morphological Control, *Chem. Mater.* 29 (2017) 4341–4350, <https://doi.org/10.1021/acs.chemmater.7b00694>.
- [40] S. Najafishirtari, R. Brescia, P. Guardia, S. Marras, L. Manna, M. Colombo, Nanoscale Transformations of Alumina-Supported AuCu Ordered Phase Nanocrystals and Their Activity in CO Oxidation, *ACS Catal.* 5 (2015) 2154–2163, <https://doi.org/10.1021/cs501923x>.
- [41] M. Comotti, W.C. Li, B. Spliethoff, F. Schüth, Support effect in high activity gold catalysts for CO oxidation, *J. Am. Chem. Soc.* 128 (2006) 917–924, <https://doi.org/10.1021/ja0561441>.
- [42] O.S.G.P. Soares, J.J.M. Órfão, J. Ruiz-Martínez, J. Silvestre-Albero, A. Sepúlveda-Escribano, M.F.R. Pereira, Pd-Cu/AC and Pt-Cu/AC catalysts for nitrate reduction with hydrogen: Influence of calcination and reduction temperatures, *Chem. Eng. J.* 165 (2010) 78–88, <https://doi.org/10.1016/j.cej.2010.08.065>.
- [43] G. Kresse, J. Furthmüller, Efficient iterative schemes for ab initio total-energy calculations using a plane-wave basis set, *Phys. Rev. B* 54 (1996) 11169–11186, <https://doi.org/10.1103/PhysRevB.54.11169>.
- [44] J.P. Perdew, K. Burke, M. Ernzerhof, Generalized gradient approximation made simple, *Phys. Rev. Lett.* 77 (1996) 3865–3868, <https://doi.org/10.1103/PhysRevLett.77.3865>.
- [45] P.E. Blöchl, Projector augmented-wave method, *Phys. Rev. B* 50 (1994) 17953–17979, <https://doi.org/10.1103/PhysRevB.50.17953>.
- [46] W. Kohn, L.J. Sham, Self-Consistent Equations Including Exchange and Correlation Effects, *Phys. Rev.* 140 (1965) A1133–A1138, <https://doi.org/10.1103/PhysRev.140.A1133>.
- [47] S. Grimme, J. Antony, S. Ehrlich, H. Krieg, A consistent and accurate ab initio parametrization of density functional dispersion correction (DFT-D) for the 94 elements H–Pu, *J. Chem. Phys.* 132 (2010) 154104, <https://doi.org/10.1063/1.3382344>.
- [48] A.P. Sutton, J. Chen, Long-range Finnis-Sinclair potentials, *Philos. Mag. Lett.* 61 (1990) 139–146, <https://doi.org/10.1080/09500839008206493>.
- [49] H. Rafii-Tabar, A.P. Sutton, Long-range Finnis-Sinclair potentials for f.c.c. metallic alloys, *Philos. Mag. Lett.* 63 (1991) 217–224, <https://doi.org/10.1080/09500839108205994>.
- [50] A.R. Denton, N.W. Ashcroft, Vegard's law, *Phys. Rev. A* 43 (1991) 3161–3164, <https://doi.org/10.1103/PhysRevA.43.3161>.
- [51] H. Li, S. Guo, K. Shin, M.S. Wong, G. Henkelman, Design of a Pd-Au Nitrite Reduction Catalyst by Identifying and Optimizing Active Ensembles, *ACS Catal.* 9 (2019) 7957–7966, <https://doi.org/10.1021/acscatal.9b02182>.

- [52] K. Mathew, R. Sundararaman, K. Letchworth-Weaver, T.A. Arias, R.G. Hennig, Implicit solvation model for density-functional study of nanocrystal surfaces and reaction pathways, *J. Chem. Phys.* 140 (2014) 084106, <https://doi.org/10.1063/1.4865107>.
- [53] K. Mathew, V.S.C. Kolluru, S. Mula, S.N. Steinmann, R.G. Hennig, Implicit self-consistent electrolyte model in plane-wave density-functional theory, *J. Chem. Phys.* 151 (2019) 234101, <https://doi.org/10.1063/1.5132354>.
- [54] J.W.M. Frenken, P. Stoltze, Are Vicinal Metal Surfaces Stable? *Phys. Rev. Lett.* 82 (1999) 3500–3503, <https://doi.org/10.1103/PhysRevLett.82.3500>.
- [55] E. Ringe, R.P. Van Duyne, L.D. Marks, Wulff construction for alloy nanoparticles, *Nano Lett.* 11 (2011) 3399–3403, <https://doi.org/10.1021/nl2018146>.
- [56] K. Heinemann, H. Poppe, In-situ TEM evidence of lattice expansion of very small supported palladium particles, *Surf. Sci.* 156 (1985) 265–274, [https://doi.org/10.1016/0039-6028\(85\)90583-7](https://doi.org/10.1016/0039-6028(85)90583-7).
- [57] C. Srivastava, S. Chithra, K.D. Malviya, S.K. Sinha, K. Chattopadhyay, Size dependent microstructure for Ag-Ni nanoparticles, *Acta Mater.* 59 (2011) 6501–6509, <https://doi.org/10.1016/j.actamat.2011.07.022>.
- [58] K. Cheirmadurai, S. Biswas, R. Murali, P. Thanikaivelan, Green synthesis of copper nanoparticles and conducting nanobiocomposites using plant and animal sources, *RSC Adv.* 4 (2014) 19507–19511, <https://doi.org/10.1039/c4ra01414f>.
- [59] J.F. Watts, J. Wolstenholme, An Introduction to Surface Analysis by XPS and AES, Wiley., 2003, <https://doi.org/10.1002/0470867930>.
- [60] N.H. Turner, B.I. Dunlap, R.J. Colton, Surface analysis: X-ray photoelectron spectroscopy, auger electron spectroscopy, and secondary ion mass spectrometry, *Fundam. Rev* (56 0) (1984).
- [61] S. Oswald, R. Reiche, M. Zier, S. Baunack, K. Wetzig, Depth profile and interface analysis in the nm-range, *Appl. Surf. Sci.* 252 (2005) 3–10, <https://doi.org/10.1016/j.apsusc.2005.01.102>.
- [62] D.C. Harris, Quantitative Chemical Analysis, 7th ed., W. H. Freeman and Company., New York, NY, 2007.
- [63] M.C. Militello, S.J. Simko, Elemental Palladium by XPS, *Surf. Sci. Spectra* 3 (1994) 387–394, <https://doi.org/10.1116/1.1247783>.
- [64] M. Brun, A. Berthet, J.C. Bertolini, XPS, AES and Auger parameter of Pd and PdO, *J. Electron Spectros. Relat. Phenom.* 104 (1999) 55–60, [https://doi.org/10.1016/s0368-2048\(98\)00312-0](https://doi.org/10.1016/s0368-2048(98)00312-0).
- [65] S.W. Gaarenstroom, N. Winograd, Initial and final state effects in the ESCA spectra of cadmium and silver oxides, *J. Chem. Phys.* 67 (1977) 3500–3506, <https://doi.org/10.1063/1.435347>.
- [66] L.H. Tjeng, M.B.J. Meinders, J. van Elp, J. Ghijssen, G.A. Sawatzky, R.L. Johnson, Electronic structure of Ag₂O, *Phys. Rev. B* 41 (1990) 3190–3199, <https://doi.org/10.1103/PhysRevB.41.3190>.
- [67] C.D. Wagner, A.V. Naumkin, A. Kraut-Vass, J.W. Allison, C.J. Powell, J.R. Rumble, NIST X-ray Photoelectron Spectroscopy, Database, Version 4 (2012) 1, <https://doi.org/10.18434/T4T88K>.
- [68] M.C. Biesinger, Silver, X-Ray Photoelectron Spectrosc. Ref. Pages. (2021). (<http://www.xpsfitting.com/>) (accessed May 20, 2022).
- [69] J.S. Bradley, G.H. Via, L. Bonnevot, E.W. Hill, Infrared and EXAFS study of compositional effects in nanoscale colloidal palladium-copper alloys, *Chem. Mater.* 8 (1996) 1895–1903, <https://doi.org/10.1021/cm960093c>.
- [70] M.C. Biesinger, L.W.M. Lau, A.R. Gerson, R.S.C. Smart, Resolving surface chemical states in XPS analysis of first row transition metals, oxides and hydroxides: Sc, Ti, V, Cu and Zn, *Appl. Surf. Sci.* 257 (2010) 887–898, <https://doi.org/10.1016/j.apsusc.2010.07.086>.
- [71] M.C. Biesinger, Advanced analysis of copper X-ray photoelectron spectra, *Surf. Interface Anal.* 49 (2017) 1325–1334, <https://doi.org/10.1002/sia.6239>.
- [72] L. Vitos, A.V. Ruban, H.L. Skriver, J. Kollár, The surface energy of metals, *Surf. Sci.* 411 (1998) 186–202, [https://doi.org/10.1016/S0039-6028\(98\)00363-X](https://doi.org/10.1016/S0039-6028(98)00363-X).
- [73] J.K. Nørskov, J. Rossmeisl, A. Logadottir, L. Lindqvist, J.R. Kitchin, T. Bligaard, H. Jónsson, Origin of the overpotential for oxygen reduction at a fuel-cell cathode, *J. Phys. Chem. B* 108 (2004) 17886–17892, <https://doi.org/10.1021/jp047349j>.
- [74] J. Rossmeisl, Z.W. Qu, H. Zhu, G.J. Kroes, J.K. Nørskov, Electrolysis of water on oxide surfaces, *J. Electroanal. Chem.* 607 (2007) 83–89, <https://doi.org/10.1016/j.jelechem.2006.11.008>.
- [75] P. Liu, J.K. Nørskov, Ligand and ensemble effects in adsorption on alloy surfaces, *Phys. Chem. Chem. Phys.* 3 (2001) 3814–3818.
- [76] H. Li, K. Shin, G. Henkelman, Effects of ensembles, ligand, and strain on adsorbate binding to alloy surfaces, *J. Chem. Phys.* 149 (2018) 1–8, <https://doi.org/10.1063/1.5053894>.
- [77] H. Li, W. Chai, G. Henkelman, Selectivity for ethanol partial oxidation: The unique chemistry of single-atom alloy catalysts on Au, Ag, and Cu(111), *J. Mater. Chem. A* 7 (2019) 23868–23877, <https://doi.org/10.1039/c9ta04572d>.
- [78] H. Li, L. Luo, P. Kunal, C.S. Bonifacio, Z. Duan, J.C. Yang, S.M. Humphrey, R. M. Crooks, G. Henkelman, Oxygen Reduction Reaction on Classically Immiscible Bimetallics: A Case Study of RhAu, *J. Phys. Chem. C* 122 (2018) 2712–2716, <https://doi.org/10.1021/acs.jpcc.7b10974>.
- [79] P. Kittisakmontree, B. Pongthawornsakun, H. Yoshida, S.I. Fujita, M. Arai, J. Panpranon, The liquid-phase hydrogenation of 1-heptyne over Pd-Au/TiO₂ catalysts prepared by the combination of incipient wetness impregnation and deposition-precipitation, *J. Catal.* 297 (2013) 155–164, <https://doi.org/10.1016/j.jcat.2012.10.007>.
- [80] A.S.G.G. Santos, J. Restivo, C.A. Orge, M.F.R. Pereira, O.S.G.P. Soares, Design of macrostructured bimetallic MWCNT catalysts for multi-phasic hydrogenation in water treatment with pre- and post-coating metal phase impregnation, *Appl. Catal. A* 643 (2022) 118790, <https://doi.org/10.1016/j.apcata.2022.118790>.
- [81] A.G. Gonçalves, J.J.M. Órfão, M.F.R. Pereira, Ozonation of sulfamethoxazole promoted by MWCNT, *Catal. Commun.* 35 (2013) 82–87, <https://doi.org/10.1016/j.catcom.2013.02.012>.
- [82] J.M.C.B. da Costa, J.R.M. Barbosa, J. Restivo, C.A. Orge, A. Nogueira, S. Castro-Silva, M.F.R. Pereira, O.S.G.P. Soares, Engineering of nanostructured carbon catalyst supports for the continuous reduction of bromate in drinking water, *C. -J. Carbon Res.* 8 (2022), <https://doi.org/10.3390/c8020021>.